

Effect of rocket exhaust of canisterized missile on adjoining launching system

Proc IMechE Part G:
J Aerospace Engineering
0(0) 1–13
© IMechE 2016
Reprints and permissions:
sagepub.co.uk/journalsPermissions.nav
DOI: 10.1177/0954410016662064
uk.sagepub.com/jaero



MSR Chandra Murty, PK Sinha and D Chakraborty

Abstract

Transient numerical simulations are carried out to study missile motion in a vertical launch system and to estimate the effect of missile exhaust in the adjoining launch structure. Three-dimensional Navier–Stokes equations along with $k-\epsilon$ turbulence model and species transport equations are solved using commercial computational fluid dynamics software. Dynamic grid movement is adopted and one degree of freedom trajectory equations are integrated with the computational fluid dynamic solver to obtain the instantaneous position of the missile. Multi-zone grid generation approach with sliding interface method through layering technique is adopted to address the changing boundary problem. The computational methodology is applied to study the missile motion in a scale-down test configuration as well as in the flight condition. The computations capture all essential flow features of test and flight conditions in active cell as well as in adjacent cells. Parametric studies are conducted to study the effect geometrical features and measurement uncertainty in the input data. Computed pressures in the adjacent cells in the launch system match better ($\sim 12\%$) with the experimental and flight results compared to distant cells.

Keywords

Universal vertical launch system, computational fluid dynamics, muzzle blast wave

Date received: 21 December 2015; accepted: 1 July 2016

Introduction

Two types of missile launching systems are generally employed in combat ships. In the first type, one or two missiles are put in a launcher which is rotated to point the missile towards the target, and the remaining missiles are stored inside the ship. In the second type of launcher, vertical canisters are employed to store and maintain all the missiles in ready to fire condition. Vertically launched canisterized missiles are operationally very convenient. Both hot launching and soft launching, and combination of the two are employed to eject the missile from the canister. For the hot launching case, the rocket motor is fired within the canister and the exhaust of rocket motor collected in a gas gathering tank before it is let out in the atmosphere through suitable uptake. Compact Vertical Launch System (VLS) needs to contain the initial impact of the rocket jet plume and safely discharge the rocket exhaust gas quickly away from the launch installations during firings of the missiles which requires innovative mechanical design and good understanding of exhaust plume characteristics.^{1–4} In the soft launching case, the hot rocket exhausts are avoided and the missile is pushed from the bottom by high pressure gas from gas generators (GG).^{5–8} In combined hot and soft launch option, initial missile movement is achieved through pressure

built up from GG and the missile is fired during its motion in the canister.

The fluid dynamic process inside and outside the canister is transient in nature. While the flow process inside the canister resembles the pressure wave generation in a closed vessel, the wave structure of the exhaust gases during missile leaving the canister is similar to that of blast wave. Blast wave development process during missile exiting the canister tube is explained by Romine and Edquist⁹ and is reproduced in Figure 1. Immediately after missile ejection from the canister, high pressure internal gases expand into the surrounding air and a complex flow field including shocks, contact surfaces, jets, etc. is formed. Although the flow field of the muzzle blast from the gun is studied extensively^{10–13} in the literature, the flow field investigations in the canister launched missile is very limited. The blast wave flow field from the gun is mostly axial dominated along the barrel axis, while

Directorate of Computational Dynamics, Defence Research and Development Laboratory, Hyderabad India

Corresponding author:

Debasis Chakraborty, Directorate of Computational Dynamics, Defence Research and Development Laboratory, Kanchanbagh P.O., Hyderabad 500058, India.
Email: debasis_cfd@drdl.drdo.in

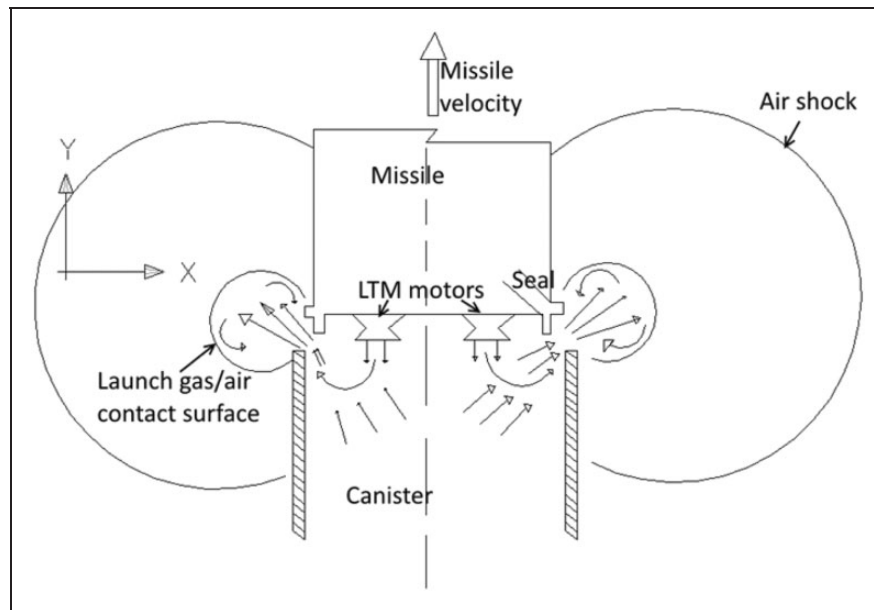


Figure 1. Flow field schematic for the missile leaving the canister.

the flow field of canister launched missile is more dependent on the geometry of the opening for gas outflow. The flow first expands radially outward through the throat formed at the annular opening and axially directed outflow develops when the annular gap exceeds the canister exit area. Till the flow develops into axial flow, it is dominated by radial blast wave development process.

Due to flow and geometrical complexities of the problem, computational fluid dynamic (CFD) methods can be used as an efficient design tool to study missile ejection from canister. Although good progresses are made in CFD methods including numerical algorithms and computing hardware for various non-reacting and reacting flow problems, the applications of CFD methods in missile ejection from canister remain very limited. Romine and Edquist⁹ have studied numerically the blast wave formation problem for the missile launched from canister using 2D/axisymmetric finite difference Eulerian code 'Shell'.¹⁴ The motion of the solid boundaries within the grid is accounted for. Lee¹⁵ has developed a mathematical model by solving unsteady Euler equations by the finite difference method based on the method of characteristics to simulate the initial transient response of the missile launch-tube gas flow and its interactions with the structural components when the rocket motor is fired. Numerical solutions compare well with the available pressure measurements and the flash X-ray photographs. Liu and Xi⁸ analyzed the gas dynamics of canister launched missiles using Fluent Software and obtained reasonable match with the test data.

The schematic of vertically launched canister system mounted on a ship and the schematic of launch scenario are shown in Figures 2 and 3,

respectively. The canister cage system contains eight missiles stored in a pressure tight canister and covered with an upper structure which has hatch cover for each missile cell. The internal arrangement of the flow path between the missile and the canister system is also shown in the same figure. There exists a closed volume between canister exit plane and hatch plane in the direction of missile motion. Before firing of any missile, hatch cover of the corresponding cell is opened. The launch of the missile is initiated with canister pressurization using gas generators. Four Low Thrust Motors (LTM) located near the main booster rocket motor base are also fired within the canister to assist the upward movement of the missile. As the missile comes out of the canister, the high pressure mixture of GG gases and LTM exhaust gases come out of the gap, formed between the canister exit and the missile base. The pressure wave travels into the adjacent cells through flow path between sleeve and bulkhead. The throat location changes from the annular gap between the canister and missile to the flow path between sleeve and bulkhead and finally to the upper annular exit area. This results in blast wave development within the sleeve as well as in the adjacent chambers. The pressure build-up in the adjacent hatch plates is high enough to open up the hatches of the cells adjacent to the active canister. Experimental studies¹⁶ were performed to examine gas dynamic shock-wave effect on launcher during missile launch.

In the present work, three-dimensional Navier–Stokes equations are solved using commercial CFD software Ansys Fluent¹⁷ to simulate the flow development process in the canister. Dynamic grid movement is adopted and Newton's 1D force balance equation is modelled through User-Defined Function (UDF) and

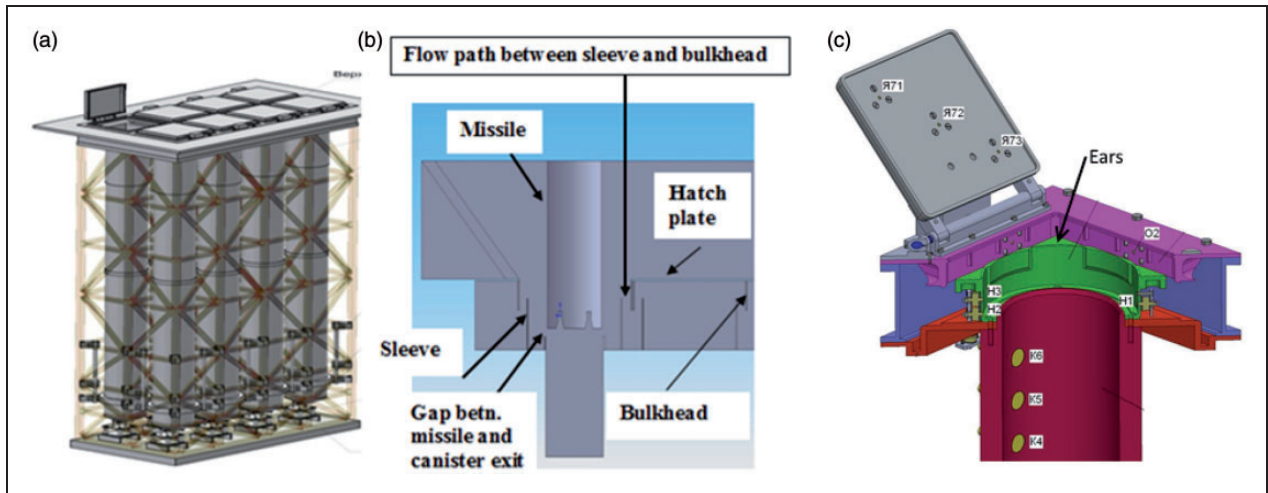


Figure 2. UVLM Geometry, (a) Model of the UVLM, (b) flow path between adjacent cells, and (c) cut section showing the sleeve ears.

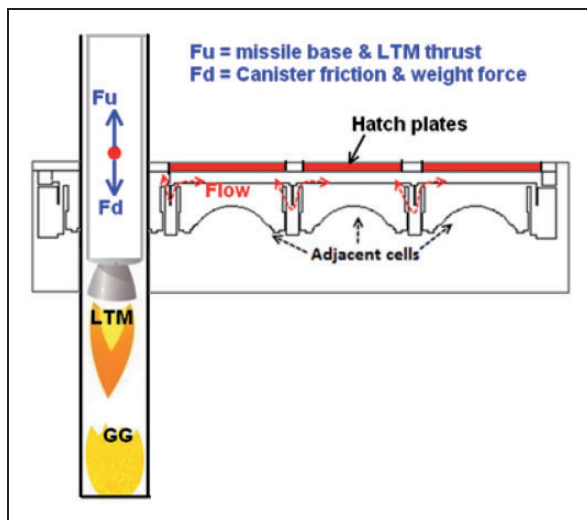


Figure 3. Schematic of present case with canister and UVLM.

integrated with the CFD solver to obtain the instantaneous position of the missile. Multi-zone grid generation approach with sliding interface method through layering technique is adopted to address the changing boundary problem. The computational methodology is first validated¹⁸ for muzzle exit velocity of bullet with experimentally measured values. The validated computational tool is then applied to study the missile motion in the canister for the experimental condition¹⁶ as well as for the flight case.

Analysis

3-D Reynolds-averaged unsteady Navier–Stokes equations with $k-\epsilon$ turbulence model with species transport equation (air and rocket exhaust) are solved. A density-based explicit solver with second-order spatially accurate Roe-Flux Difference Splitting Scheme¹⁹ is used for spatial discretization.

First-order Euler discretization is used for temporal terms with dual time inner loop iterations of 40. Every time step is converged to four decade fall in RMS residuals with a maximum CFL number of 0.8.

Governing equations

The appropriate system of equations that governed the turbulent compressible gas may be written as follow:

Continuity equation

$$\frac{\partial \rho}{\partial t} + \frac{\partial}{\partial x_k} (\rho u_k) = 0 \quad k = 1, 2, 3. \quad (1)$$

Momentum equation

$$\frac{\partial}{\partial t} (\rho u_i) + \frac{\partial}{\partial x_k} (\rho u_i u_k) + \frac{\partial p}{\partial x_i} = \frac{\partial (\tau_{ik})}{\partial x_i}, \quad i, k = 1, 2, 3. \quad (2)$$

Energy equation:

$$\frac{\partial}{\partial t} (\rho E) + \frac{\partial}{\partial x_k} (\rho u_k H) = \frac{\partial}{\partial x_k} (u_j \tau_{jk}) + \frac{\partial q_k}{\partial x_k}, \quad j, k = 1, 2, 3. \quad (3)$$

Species mass fraction (z)

$$\frac{\partial}{\partial t} (\rho z) + \frac{\partial}{\partial x_k} (\rho u_k z) = \frac{\partial}{\partial x_k} \left(\left(\frac{\mu_l}{Pr} + \frac{\mu_t}{\sigma_c} \right) \frac{\partial z}{\partial x_k} \right) \quad (4)$$

where ρ , u_i , p , E , and H are the density, velocity components, pressure, total energy, and enthalpy respectively.

In eddy viscosity models, the stress tensor is expressed as a function of turbulent viscosity (μ_t). Based on dimensional analysis, turbulent kinetic energy (K) and turbulent dissipation rate (ε) are defined as follow

$$k = \overline{u'_i u'_i} / 2 \quad \varepsilon \equiv \nu \frac{\partial u'_i}{\partial x_j} \left(\frac{\partial u'_i}{\partial x_j} + \frac{\partial u'_j}{\partial x_i} \right). \quad (5)$$

Turbulent kinetic energy (K) equation

$$\frac{\partial}{\partial t} (\rho K) + \frac{\partial}{\partial x_k} (\rho u_k K) = \frac{\partial}{\partial x_k} \left(\left(\frac{\mu_l}{Pr} + \frac{\mu_t}{\sigma_K} \right) \frac{\partial K}{\partial x_k} \right) + S_K. \quad (6)$$

Rate of dissipation of turbulent kinetic energy (ε) equation

$$\frac{\partial}{\partial t} (\rho \varepsilon) + \frac{\partial}{\partial x_k} (\rho u_k \varepsilon) = \frac{\partial}{\partial x_k} \left(\left(\frac{\mu_l}{Pr} + \frac{\mu_t}{\sigma_\varepsilon} \right) \frac{\partial \varepsilon}{\partial x_k} \right) + S_\varepsilon \quad (7)$$

where $\mu = \mu_l + \mu_t$ is the total viscosity; μ_l, μ_t being the laminar and turbulent viscosity and Pr is the Prandtl number. The source terms S_K and S_ε of the K and ε equation are defined as

$$S_K = \tau_{ik} \frac{\partial u_i}{\partial x_k} - \rho \varepsilon \quad \text{and} \quad S_\varepsilon = C_{\varepsilon 1} \tau_{ik} \frac{\partial u_i}{\partial x_k} - C_{\varepsilon 2} \frac{\rho \varepsilon^2}{K}$$

where the turbulent shear stress is defined as

$$\tau_{ik} = \mu_t \left(\frac{\partial u_i}{\partial x_k} + \frac{\partial u_k}{\partial x_i} \right).$$

Laminar viscosity (μ_l) is calculated from Sutherland law as

$$\mu_l = \mu_{ref} \left(\frac{T}{T_{ref}} \right)^{3.2} \left(\frac{T_{ref} + S}{T + S} \right)$$

where T is the temperature and μ_{ref}, T_{ref} and S are known values. The turbulent viscosity μ_t is calculated as

$$\mu_t = c_\mu \frac{\rho K^2}{\varepsilon}.$$

The coefficients involved in the calculation of μ_t are taken as

$$c_\mu = 0.09, \quad C_{\varepsilon 1} = 1.44, \quad C_{\varepsilon 2} = 1.92 \\ \sigma_K = 1.0, \quad \sigma_\varepsilon = 1.3, \quad \sigma_c = 0.9.$$

The heat flux q_k is calculated as $q_k = -\lambda \frac{\partial T}{\partial x_k}$, where λ is the thermal conductivity.

Grid generation and mesh motion

Since the domain boundaries are changing with time, 'multi-zone with sliding interface' grid generation approach is adopted. Separate computational mesh is generated for missile path and rest of the domain, as shown in Figure 4. During missile motion, two zones are integrated fluid dynamically through sliding interface boundary condition. Whenever the missile changes its position, layers of mesh are created in inlet (missile base) region while layers are removed at the other end (outlet) as shown in Figure 4. A 1DOF routine is developed for missile motion and integrated with CFD solver to find the new position of the missile, and the mesh is moved dynamically.

$$\frac{d}{dt} \int_V \rho \phi dV + \int_{\partial V} \rho \phi (\vec{u} - \vec{u}_g) \cdot d\vec{A} \\ = \int_{\partial V} \Gamma \nabla \phi \cdot d\vec{A} + \int_V S_\phi dV \quad (8)$$

where u_g is the grid velocity

$$\int_{t_0}^t dv = \int_{t_0}^t (F/m) dt. \quad (9)$$

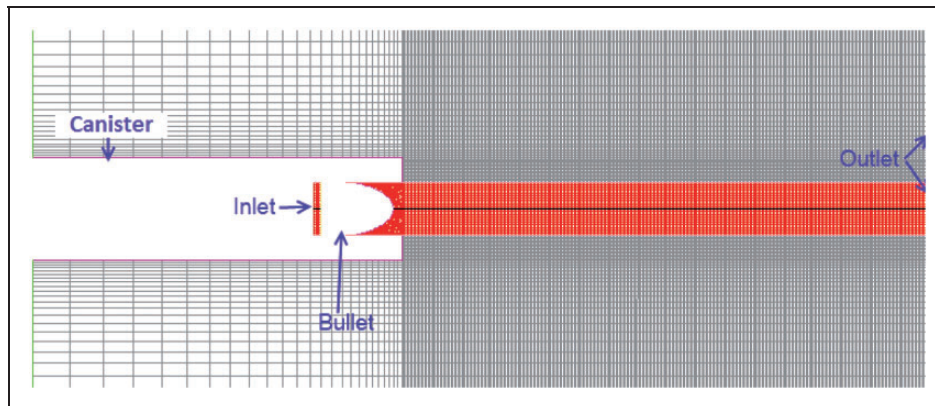


Figure 4. Computational mesh close to missile.

Here, F is the resultant force acting on missile, including pressure force on missile base, LTM thrust, gravity force, and drag force. m is instantaneous missile mass corrected with exhausted propelled gas.

The instantaneous missile velocity is obtained as follows

$$v_t = v_{t-\Delta t} + (F/m)\Delta t. \quad (10)$$

In the CFD solver,¹⁷ dynamic meshing is implemented through layering. According to this method, a computational cell is split into two, if the size of the cell (h) meets the criteria $h > (1 + \alpha_s) h_{ideal}$. Similarly, two adjacent cells collapse into single cell upon meeting the criteria $h < \alpha_c h_{ideal}$ (see Figure 5). α_s and α_c are the split factor and collapse factor. The values of h_{ideal} , α_s , and α_c are determined by trial and error till the solution stabilizes. As the flow gradient is initially high and reduces subsequently, the above parameters are checked for the stability of the solution of initial motion. Further simulation is done by fixing these parameters for a given problem.

Simulation of scale-down test configuration

Description of experimental setup

To understand and resolve the high hatch pressure levels, a scale down (1:6.7) model of the launch mechanism was tested and the results are documented in literature.¹⁶ A number of experiments were conducted to finalize (1) optimal weight of missile model, (2) canister pressure at missile exit, (3) operation mode of GG and its gas composition, (4) different sleeve configuration, (5) the effect of LTM firing on gas dynamic behavior, etc. The experimental setup is shown schematically in Figure 6. High temperature test gas is produced in GG by burning H_2 , O_2 , N_2 mixer. The diaphragm ruptures at specified pressure and pushes the missile model out of canister. The gas composition and pressure is adjusted to simulate the missile velocity at the canister exit. The test configuration contains eight cells and pressure sensors are located on each hatch cover from inside and also on canister and sleeve at different locations. Further details of the experimental condition are available in literature.¹⁶

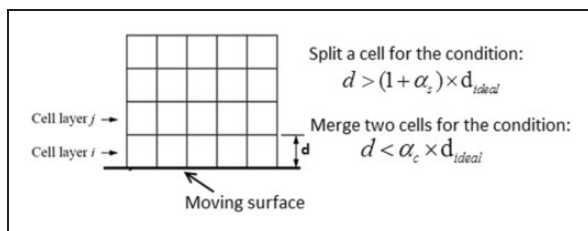


Figure 5. Mesh split/merge parameters.

Computational domain, grid and inflow parameters

Although experimental investigations are carried out for a number of cases, present simulation deals with only one case where the missile obturator clears canister exit. The computational domain is extended by about 1 m in the ambient in all sides. Good quality structured grid (Figure 7) with 2 million nodes are generated in the computational domain. Although no explicit grid independence study is done for the current problem, based on our previous experience of simulating complex flow problems, we have clustered enough grid points near the expected higher flow field gradient.

The measured pressure profile at inflow section (Figure 8) and total temperature of 3000 K is imposed in the inflow plane. Missile muzzle velocity is measured as 40 m/s. Though missile velocity is expected to change marginally during its short duration trajectory, it is fixed in the simulation as 40 m/s. Transient simulation is carried out for 30 ms with a time step of 0.1 μ s. A two-component gas (air and propellant exhaust) is considered for simulation and the mixing of hot gas with air is modelled.

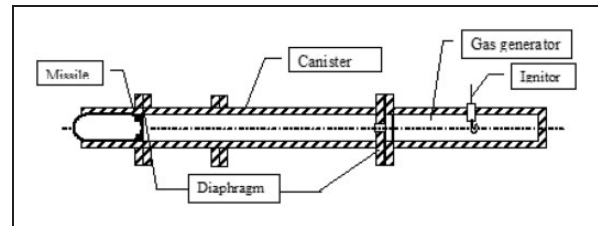


Figure 6. Schematic of experimental setup.

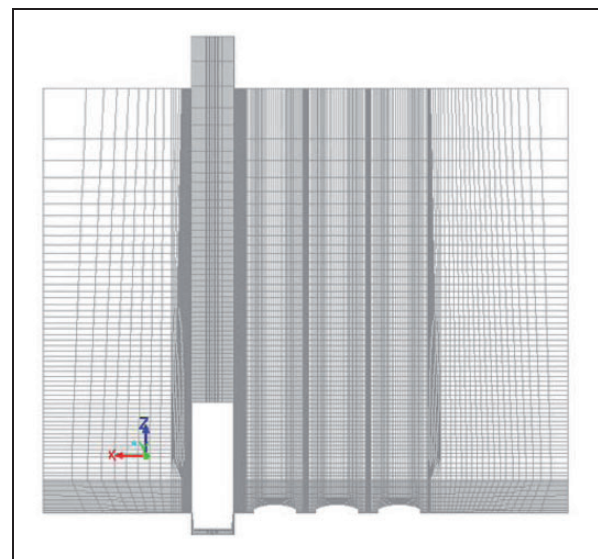


Figure 7. Grid structure in computational domain.

Results and discussion

The qualitative features of the flow development in the launch mechanism are shown through distributions of velocity vectors at different time instants ($t = 16.5, 18, 21, 25$ ms) in Figure 9. As time

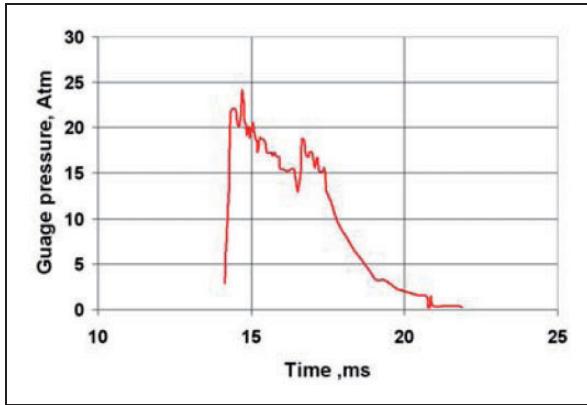


Figure 8. Pressure profile at the inflow plane.

progresses, the fluid velocities in the distant cells are becoming more and more complex, and recirculating flow patterns are developing in the active and adjoining cells. The computed pressure histories in the active cell for two locations (ac-1 & ac-2) are compared in Figure 10. Sensors ac-1 and ac-2 are located inside the canister at 16.7 and 8.4 mm measured from top of the canister, respectively.

The computations captured all essential features of the flow field. The existence of two pressure pulses (first one small, second one big), and the locations of pressure peaks are nicely captured. The computed first peak is lower than the experimental data, while the computed second peak is higher. The computed peak pressure for 'ac-1' sensor matches the experimental data nicely while that of 'ac-2' sensor overpredicts the experimental value by 12%. Four adjacent sensors (ad-1, ad-2, ad-3, and ad-4) are considered for comparison. The first two sensors (ad-1 and ad-2) are positioned in the eastern adjacent cell, the sensor ad-3 is positioned at the southern adjacent cell while the sensors ad-4 is positioned in the cell diametrically

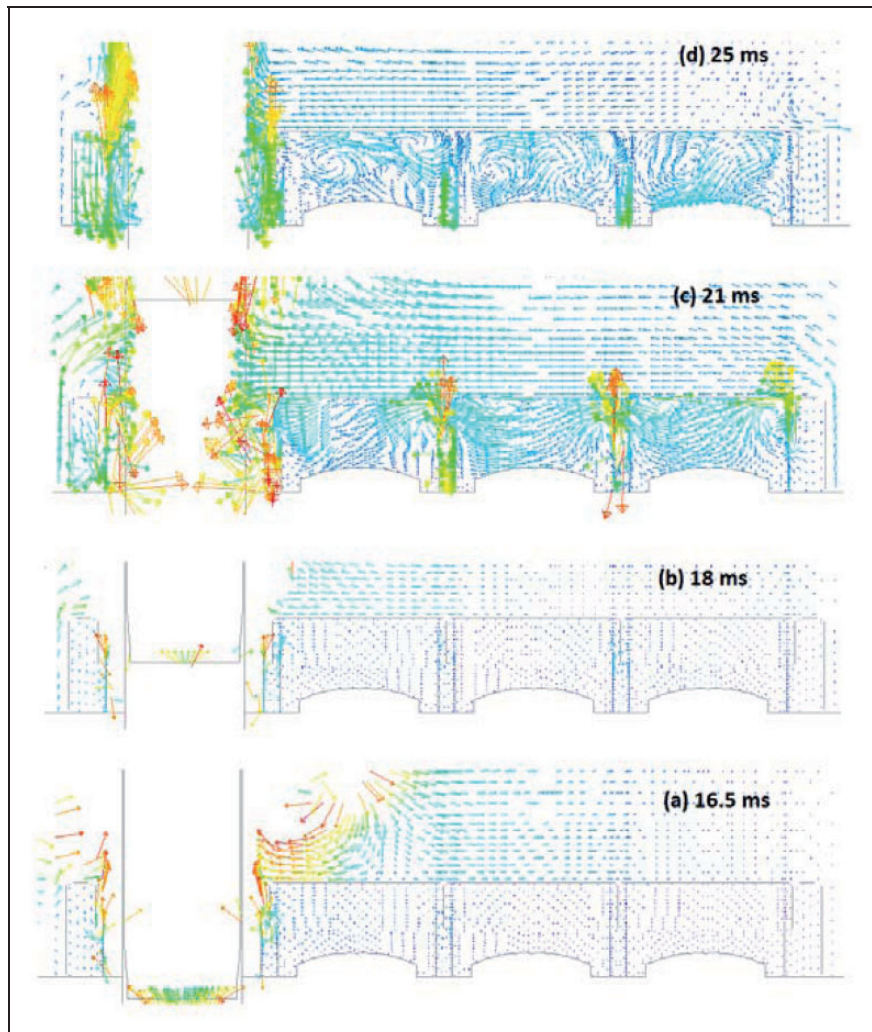


Figure 9. Velocity vector plot at different time instants.

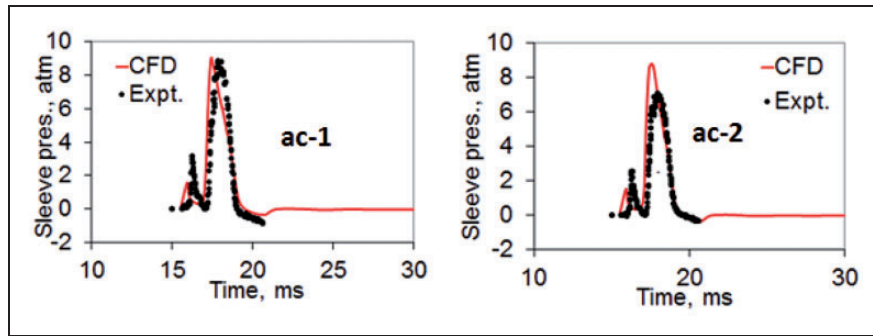


Figure 10. Pressure comparisons for active canister, ac-1 (left) and ac-2 (right).

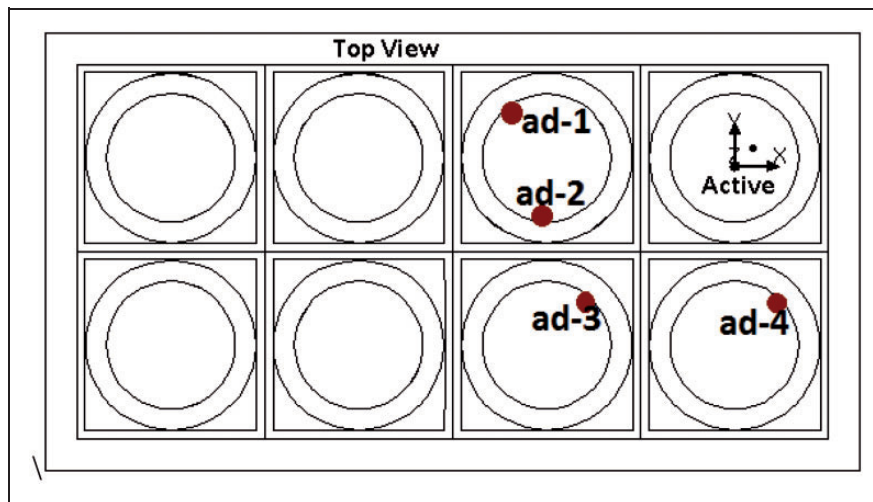


Figure 11. Measurement layout.

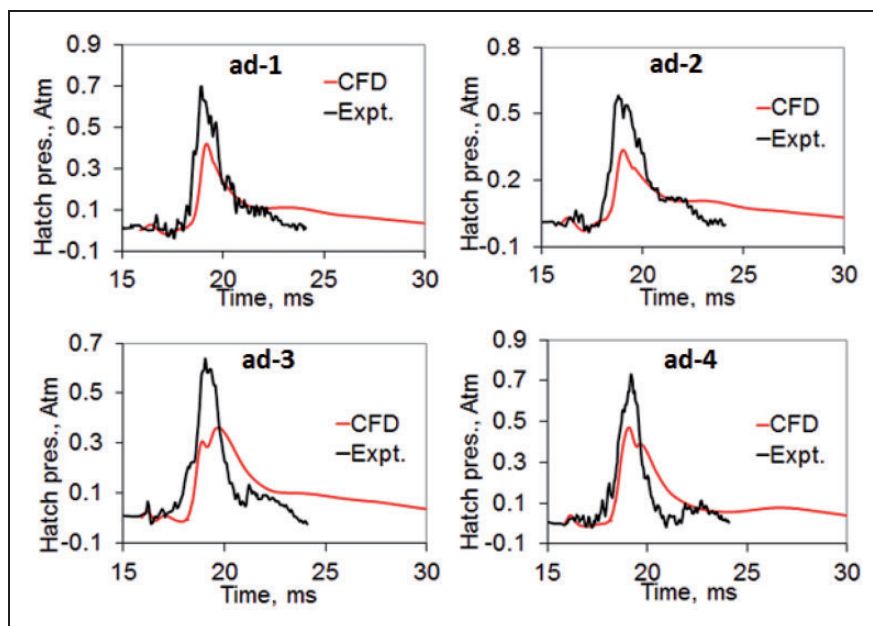


Figure 12. Pressure comparison for adjacent canister instances (a) 0.4424 s, (b) 0.4473 s, (c) 0.4503 s, and (d) 0.4543 s.

opposite to the active cell. The measurement layout of the sensors at the adjacent cells is shown in Figure 11. The computed pressure data at the adjacent cells are compared with the measurements in Figure 12. The pressure histories of the sensors at the active and adjacent cells show slightly different patterns. The first peak pressure pulse in the adjacent cell is very weak compared to the first peak in the active cell. Also, the peak magnitudes of pressure pulse in the adjacent cells are somewhat lower than the active cell pressure. The computation underpredicts the peak pressure for all the sensors by about 30–45%. The decay of computed pressure pulses is slower than the experimental value. The complexities of the geometry and uncertainties of measured inflow parameters may be the cause of these discrepancies between the computed and measured values.

Efforts were made to explain the mismatch in the pressure by studying the effect of cell-to-cell flow path and experimental measurement of missile base position. The GG gas flow takes multiple U-turns from the active cell to all other cells. In actual geometry, there are four ears on top of each sleeve that reduces the flow path area from sleeve to sleeve. The effect of these ears on the pressure history is studied by making new geometries and simulations. The missile base position error is studied by considering two time instants of 15.2 ms and 14.8 ms instead of original 15.8 ms time

instant for which the missile obturator leaves the canister exit. These cases are referred as synchronization time error of 0.6 ms and 1 ms, respectively. The pressure history at the sensor location of ‘ad-1’ for different parametric cases is compared in Figure 13. Four different cases are compared in the figure. The introduction of ‘ears’ in the sleeve is shown to reduce the peak pressure while the synchronization error of 1 ms is seen to increase the peak pressure above the experimental data. Although the experimental peak pressure could be matched with the synchronization error of 0.6 ms, the decay of computational pressure is much higher than the experimental values.

Simulation of flight condition

Computational domain and grid

The simulation methodology is applied to flight condition where the full missile and firing of LTM in the canister are also considered. The missile canister inner diameter is about 1D (D is the missile diameter). Sleeve height is about 0.5D and its inner diameter is about 1.35D. Each cell is having a 1.5D × 1.5D cross section. The dimensions of length, breadth and height of upper volume are 5.9D, 2.9D and 0.8D respectively. Atmospheric domain is extended approximately 12D in all lateral directions. The GG exhaust expands in horizontal plane and fills the canister. Multi-block

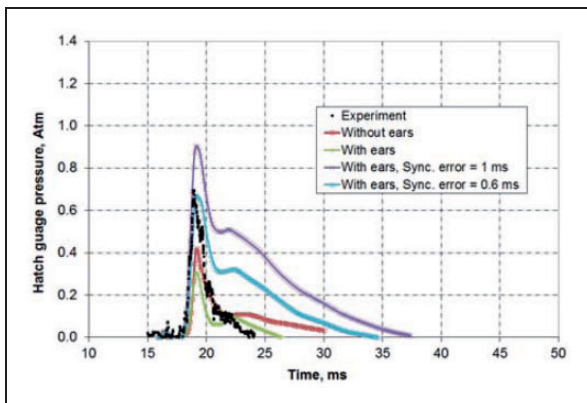


Figure 13. Parametric variation of pressure at location ‘ad-1’.

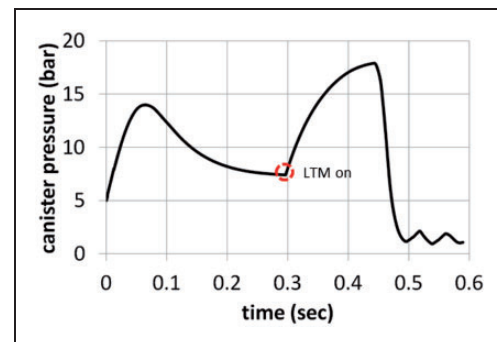


Figure 15. Canister pressure variation with time.

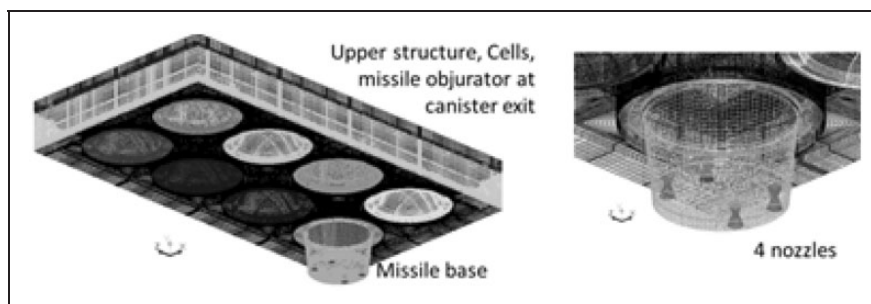


Figure 14. Structured Computational grid at different locations.

structured grid of about 2 million cells is generated in the computational domain at the start of the simulation. The grid distributions at upper structure and at the missile with four LTM nozzles are

depicted at Figure 14. As the missile moves with time, domain boundaries change with time. Grid size goes on increasing as time proceeds, due to addition of grid layers at the bottom of the missile.

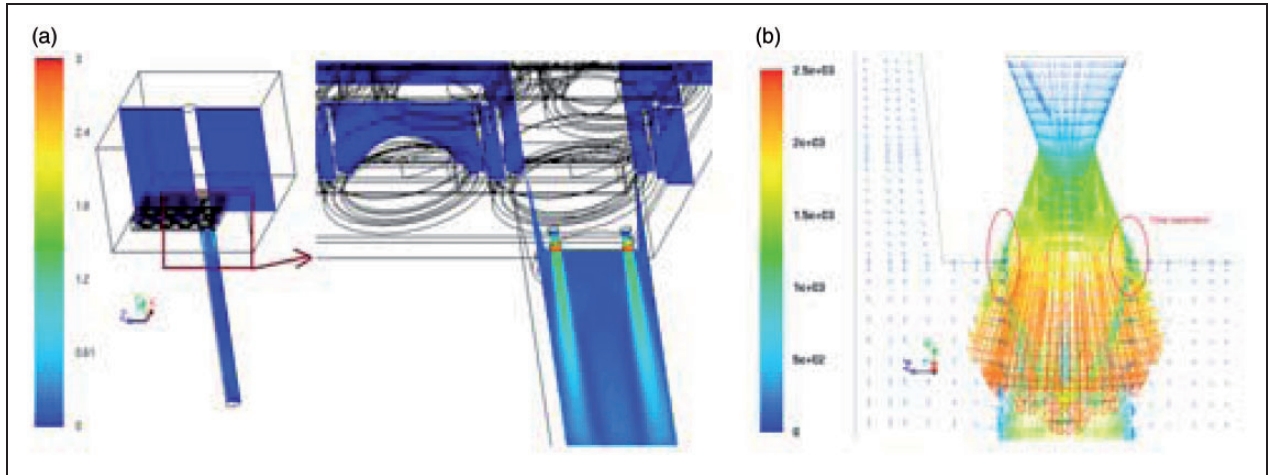


Figure 16. Flow parameters in the canister during LTM firing (44.23 ms): (a) Mach contours while LTM firing inside canister, and (b) velocity vectors in LTM nozzle.

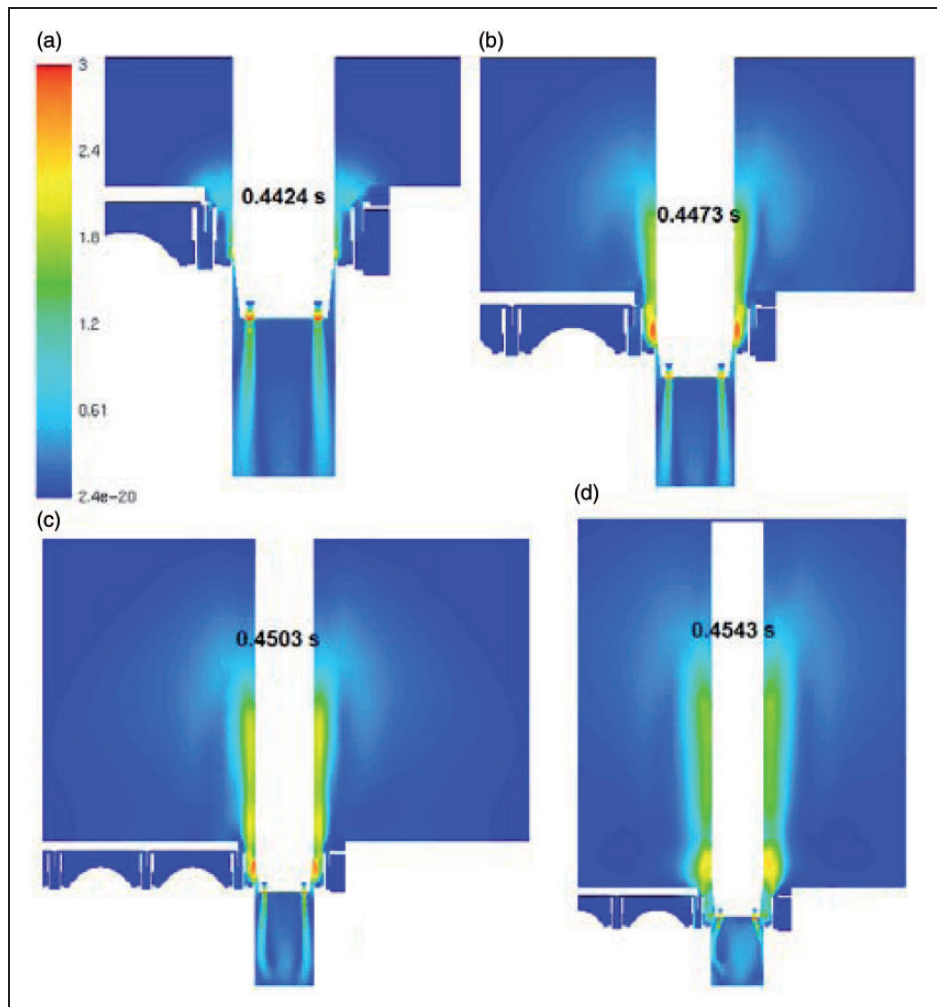


Figure 17. Mach number contour showing blast wave development process at different time instants.

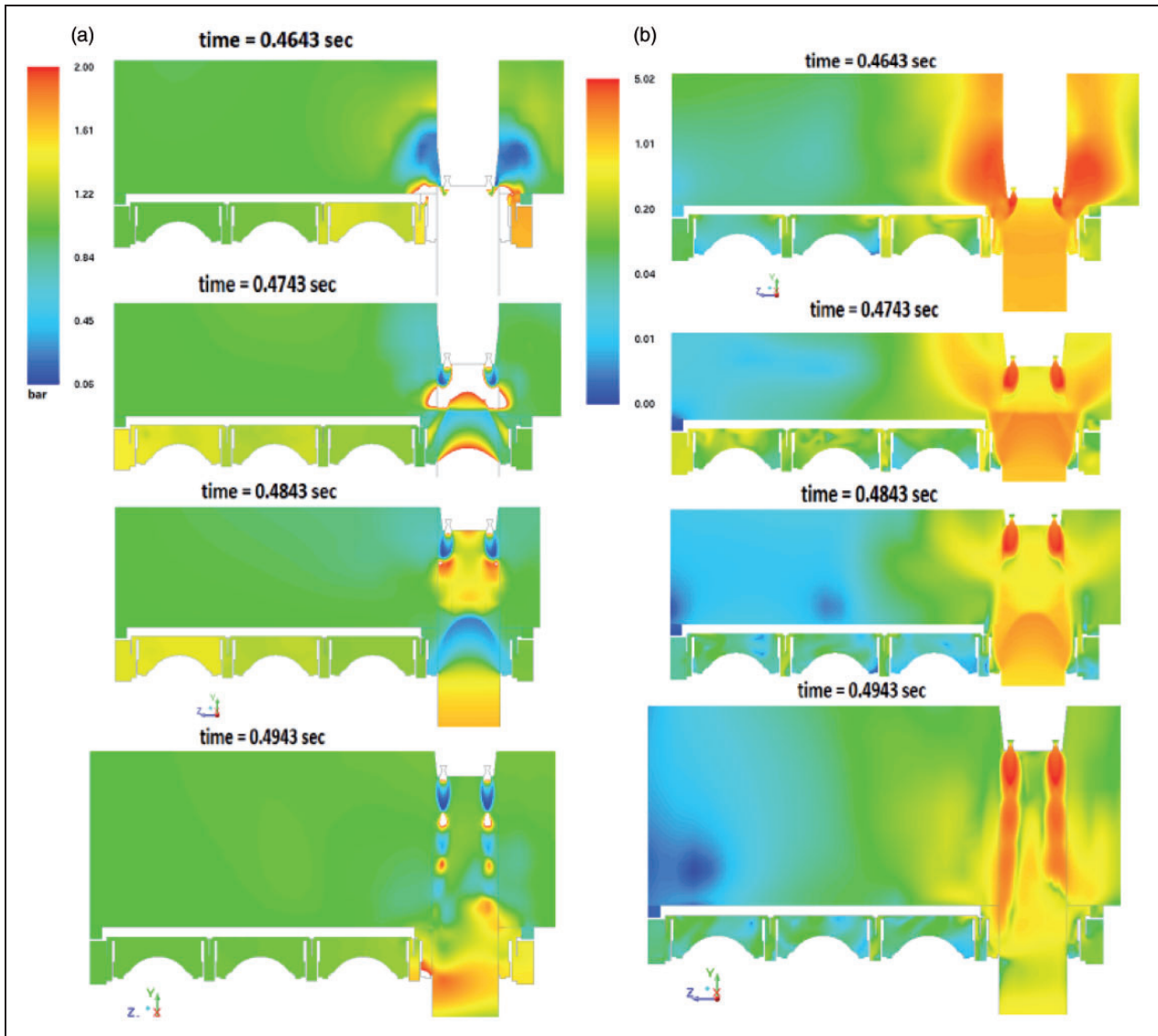


Figure 18. (a) Pressure and (b) Mach contours at four time instances (0.4643 s, 0.4743 s, 0.4843 s and 0.4943 s).

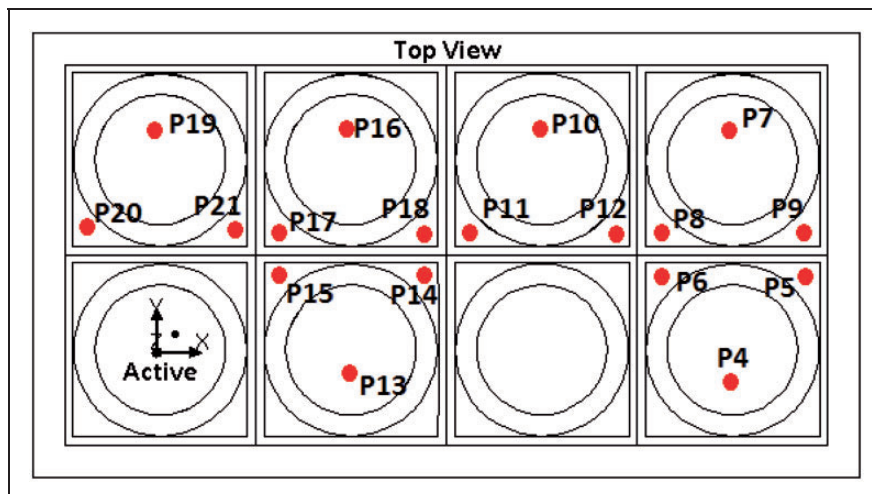


Figure 19. Measurement layout with locations of pressure sensors.

The final grid size is about 4.6 million at the end of the simulation time.

Results and discussions

Four different events of launch sequence, namely (a) initial pressure build-up by GG to start the missile motion, (b) missile motion till LTM motors start operating, (c) missile motion until obturator reaches canister exit, and (d) obturator opens to atmosphere causing active and adjacent canister flow interaction, are addressed in the simulation. Nitrogen gas is injected into the canister at temperature of 300 K for about 12.3 ms. The missile base pressure reached about 7.83 bar and missile starts moving forward in the canister. In the second phase, missile movement is modelled by 1DOF force balance equation and the missile is moved till 0.2962 s till LTM is fired. Volume-averaged canister pressure history is plotted in Figure 15. Canister pressure increased to about 14 bar at 0.6 s, and slowly reduces to about 7.5 bar by the end of the second phase when the missile attains the velocity of about 22.5 m/s. At 0.2962 s, LTM are fired and the missile experiences additional thrust and accelerates further. Canister pressure rapidly increases to about 17.8 bar (see Figure 15) and the obturator reaches canister exit at 0.4423 s.

Mach number distribution in the canister during LTM firing (at 0.4423 s) is shown in Figure 16. With the expansion of LTM nozzle flow, mixing with canister gas is clearly observed. Due to high back pressure, nozzle flow gets separated in the divergent portion of the nozzle (Figure 16 (b)). As the missile travels, the gas starts escaping into the sleeve through blast wave and the canister pressure starts falling. The Mach number contour around canister exit is shown in Figure 17 at four instances depicting the blast wave movement.

Missile base clears the canister exit at 0.453 s and the combined canister and LTM nozzle flow interact with upper structure (TSS), and in this phase the hatches get exposed to the canister flow. The high pressure and high temperature gas enter into the gaps between sleeves and bulk head structure by

taking multiple U-turns and increase the hatch under-surface pressures. The snapshots of Mach number and pressure distribution in the active cell as well as in the adjacent top structure at different time instants (46.4, 47.4, 48.4 and 49.4 ms) are shown in Figure 18. In the contour plots, the relative change in missile position with time is also observed. At time 0.4432 s, obturator just opens to atmosphere, and slowly the annular gap increases with time, and at 0.453 s, the missile base reaches the canister exit. By 0.464 s, the missile base reaches the top of the TSS. By the end of 0.494 s, the missile has reached a height of about 1.9 m from canister exit. Pressure is seen to rise on the hatch under-surface around 0.464 s time due to interaction of two opposing jets (LTM jet and canister jet) causing the diversion of flow towards sleeve–bulkhead gap. Though the pressures are high during the period it travels from canister exit to upper volume exit plane ($0.453 < t < 0.464$ s), the resultant side jet is not diverted towards sleeve–bulkhead gap due to presence of sleeve and expands to atmosphere. But, after 0.464 s, the incident angle of resultant jet is diverted to sleeve–bulkhead gap, thus causing the hatch pressure rise. We can also observe from contour plots that the resultant jet angle undergoes changes with position of missile. It is clearly observed that at around 0.47 s, the jet is directly impinging into the sleeve–bulkhead gap, and thus causes the maximum hatch pressures. This high pressure under the hatch cover plates caused the failure of latch mechanism and broke open the hatch cover plates in the initial flight trials.

Number of pressure sensors was provided in the adjacent cells of the launch mechanism to estimate the interaction of canister exit gas. The schematic of pressure sensors' locations is provided in Figure 19. The computed pressure history of the adjacent cells (p13 at cell 5, p16 at cell 6 and p22 at cell 8) is compared with flight data in Figure 20 and a reasonable good match is obtained. Although computed pressures capture the trend of the flight measured data, it is over-predicted compared to the flight measurements. However, at 0.464 s, when the missile base clears the TSS upper surface, the computation and flight measured data is closely matching.

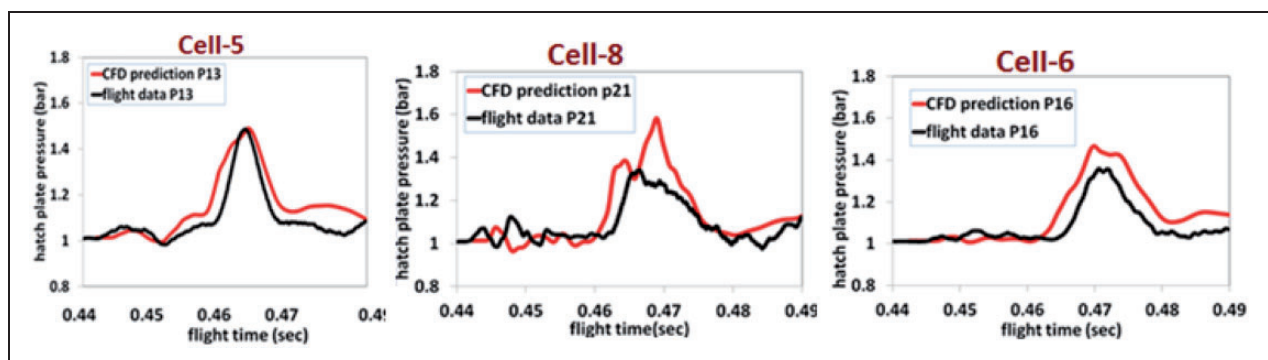


Figure 20. Comparison of hatch pressures for adjacent cells (cells 5, 6, and 8).

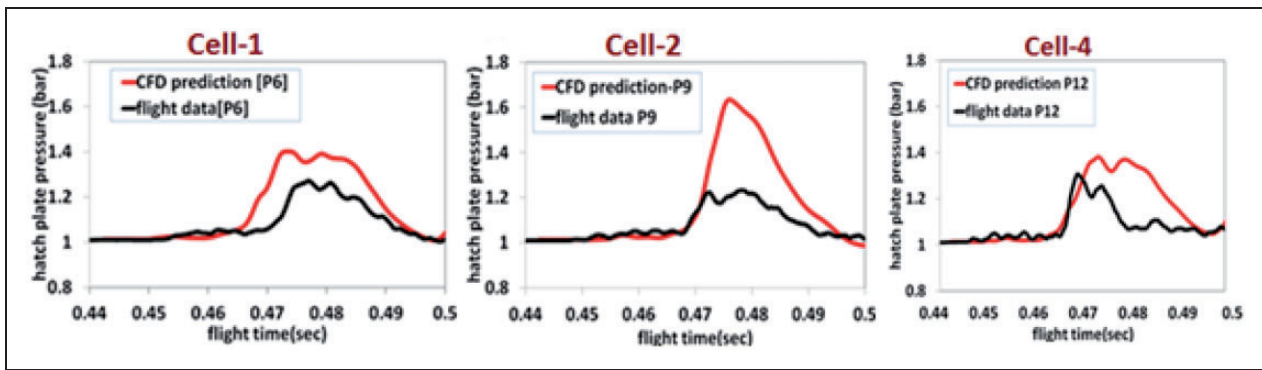


Figure 21. Comparison of hatch pressures for distant cells 1, 2, and 4.

Table 1. Comparison of peak pressures.

	Flight data	CFD prediction, bar	Difference (%)
Cell-5, P13	1.47	1.48	0.68
Cell-5, P14	1.4	1.41	0.71
Cell-5, P15	1.44	1.45	0.69
Cell-6, P16	1.32	1.42	7.58
Cell-8, P19	1.34	1.63	21.64
Cell-8, P20	1.33	1.6	20.30
Cell-8, P21	1.33	1.56	17.29
Cell-4, P12	1.3	1.38	6.15
Cell-1, P4	1.21	1.4	15.70
Cell-1, P5	1.22	1.55	27.05
Cell-1, P6	1.26	1.39	10.32
Cell-2, P7	1.27	1.66	30.71
Cell-2, P8	1.33	1.58	18.80
Cell-2, P9	1.23	1.61	30.89

The comparison of pressure histories for the far away cells (p6 at Cell 1, p9 at cell 2 and p12 at cell 4) is presented in Figure 21. The difference between the computations and flight measured data is more for the distant cells compared to the adjacent cells. Lack of better grid distributions in the distant cells and modelling uncertainty is conjectured to be the cause of these differences. No attempts are made to resolve the differences. The pressure pulse phenomenon is highly transient in nature, sustaining only 20 ms. Comparison of peak pressures between present computations and flight data for all the cells is shown in Table 1. The difference in computed and flight measured peak pressure is less for the adjacent cells compared to the distant cells. Maximum difference of about 30% is observed between the computation and flight measured data in the distant cell 2.

Conclusions

Three-dimensional transient numerical simulations are performed to understand missile motion inside the

vertical launch canister and missile exhaust interaction with adjoining launch mechanism system. RANS equations are solved for multi species along with $k-\epsilon$ turbulence model on dynamic grid framework using commercial CFD code. Dynamic mesh motion/layering technique is employed to account for missile travel. 1-D force balance equation is solved to obtain the instantaneous missile position and velocity.

Simulations are carried out for scale down test configurations as well as the flight conditions. For scale down configuration, the computed transient pressures captured the essential features of the flow field including two pressure pulses and the locations of pressure peaks. The computed peak pressures at the active cell over predict the experimental data by 12% of active cell and under predicts by 30–45% for the adjacent cells. Parametric studies with different geometries and synchronization error reveal that although the experimental peak pressure could be matched with 0.6 ms synchronization error, the decay of computational pressure is much higher than the experimental values.

For the flight configuration analysis, simulation captures all the events of launch sequence including Initial pressure build-up by GG, firing of LTM motor, missile motion until obturator reaches canister exit and the interaction between missile exhaust and adjacent canister. Due to high back pressure, nozzle flow is seen to get separated in the divergent portion of the nozzle. As the missile travels, the gas starts escaping into the sleeve through blast wave and increases the hatch under-surface pressures. It is observed that when the jet is directly impinging into the sleeve-bulkhead gap, hatch pressures are maximum. Computed pressures over-predict the flight measurements. The difference between the computations and flight measured data is about 12% for the adjacent cell and is about 30% for the distant cells. Present prediction has demonstrated that the complex transient gas dynamics during missile launching from canister is tractable.

Acknowledgement

The authors would like to express their sincere gratitude to Sri. S. Som, ex_director, DRDL for his constant

encouragement, review of results and for providing necessary test and flight data for comparison.

Declaration of Conflicting Interests

The author(s) declared no potential conflicts of interest with respect to the research, authorship, and/or publication of this article.

Funding

The author(s) received no financial support for the research, authorship, and/or publication of this article.

References

1. Fu D and Yu Y. Simulation of gas flow and additional thrust with missile launching from concentric canister launcher. In: *Proc IMechE, Part G: J Aerospace Engineering* 2013; 227: 1977–1987.
2. Lee K-S, Hong S-K and Park S-O. Supersonic jet impingement navier-stokes computations for vertical launching system design applications. *J Spacecraft Rockets* 2004; 41: 735–744.
3. Lee K-S, Hong S-K and Ahn CS. Numerical investigations of supersonic jet impingement on a flat wall in a confined plenum. In: *Proceedings of the 6th computational fluid dynamics conference*, National Taiwan University, Taipei, Taiwan, 23–27 October 2005.
4. Saha S and Chakraborty D. Plume-ducting system design of vertical launcher using computational-fluid-dynamics tools. *J Spacecraft Rocket* 2013; 50: 715–718.
5. Mckinnis JA and Oconnell AR. MX Launcher gas generator development. *J Spacecrafts Rocket* 1983; 20: 259–265.
6. Nath De T. Configuration design of spring loaded detachable canister launch vehicle interface for multi-stage long launch vehicle. *IOSR J Eng* 2012; 2: 1328–1333.
7. Rui S and Xing Y. Comparative studies of interior ballistic performance among several missile eject power systems. *J Beijing Univ Aeronaut Astronaut* 2009; 35: 766–770.
8. Liu Y and Xi A. An interior trajectory simulation of the gas-steam missile ejection. *J Computat* 2013; 8: 1321–1326.
9. Romine G and Edquist C. Muzzle blast from canister launched missiles, AIAA-1980-1187. In: *16th Joint propulsion conference*, American Institute of Aeronautics and Astronautics, 1980.
10. Erdos JI and Guidice PDD. Calculation of muzzle blast flowfields. *AIAA J* 1975; 13: 1048–1055.
11. Taylor TD and Lin TC. Numerical model for muzzle blast flowfields. *AIAA J* 1981; 19: 346–349.
12. Jiang X, Fan B and Li H. Numerical investigations on dynamic process of muzzle flow. *Appl Math Mech* 2008; 29: 351–360.
13. Cooke CH. Application of an explicit TVD scheme for unsteady, axisymmetric, muzzle brake flow. *Int J Numer Meth Fluid* 1987; 7: 621–633.
14. Moore GR. Finite difference calculations of the free-air gun blast about the muzzle of a 5in./54 Naval Gun. Virginia, USA: Naval Weapons Laboratory, 1972.
15. LEE S. Initial transient analysis of missile launch-tube gas flow and its interactions with structures. In: *29th Joint propulsion conference exhibit*, Monterey, CA, USA, American Institute of Aeronautics and Astronautics, Paper No. AIAA 93-2455, 28–30 June 1993.
16. *Experimental study of gas dynamic shock-wave affect on structural elements of launcher while launching the missile and finding ways to reduce this affect*. Russia: NPOM, 2011.
17. Ansys Fluent 14.5 theory and users guide. India: Ansys Inc, 2013.
18. Chandra Murty M and Sinha PK. Transient gas dynamic studies of projectile motion inside canister using dynamic computational mesh – a validation study. In: *Proceedings of 6th symposium on applied aerodynamics and development of aerospace vehicles (SAROD-2013)*, 21–23 November 2013, pp.644–649.
19. Roe PL. Characteristic-based schemes for the Euler equations. *Annu Rev Fluid Mech* 1986; 18: 337–365.

Appendix

Notation

E	total energy
F	force
H	total enthalpy
K	turbulent kinetic energy
p	static pressure
P_r	Prandtl number
T	static temperature
t	time
u	flow velocity
u_g	mesh velocity
x	distance
Z	species mass fraction

Subscripts

l	laminar quantity
t	turbulent quantity
i, j, k	spatial coordinates of cell indices

Greek symbols

Δ	difference operator
ε	turbulent dissipation
μ	dynamic viscosity
ρ	mass density
τ_{ij}	laminar viscous stress tensor
ϕ	conserved flux variable
∇	Del operator
∂	partial derivative